IAEA nuclear fusion

Roles of ECH system in DTT plasma operations

To cite this article: G. Granucci *et al* 2024 *Nucl. Fusion* **64** 126036

OPEN ACCESS
IOP Publishing | International Atomic Energy Agency
Nuclear Fusion
Nucl. Fusion 64 (2024) 126036 (13pp)
https://doi.org/10.1088/1741-4326/ad7742

Roles of ECH system in DTT plasma operations

G. Granucci[1,2,*], F. Auriemma[1,3], L. Aucone[8], B. Baiocchi[1], N. Bonanomi[1], F. Braghin[4], A. Bruschi[1], D. Busi[4], I. Casiraghi[1], L.E. di Grazia[7], F. Fanale[1,2], L. Figini[1], S. Garavaglia[1], P. Mantica[1], M. Mattei[6,7], A. Moro[1], S. Nowak[1], P. Platania[1], D. Ricci[1], N. Rispoli[1], A. Romano[2,5], G. Rubino[1,5], S. Schmuck[1] and A. Simonetto[1]

[1] Institute for Plasma Science and Technology—CNR, Milano, Italy
[2] DTT S.C. a r.l., Frascati (RM), Italy
[3] Consorzio RFX, Corso Stati Uniti 4, 35127 Padova, Italy
[4] Department of Mechanical Engineering, Politecnico di Milano, Milano, Italy
[5] ENEA, Fusion and Nuclear Safety Department, C.R. Frascati, Frascati, Italy
[6] CREATE, Napoli, Italy
[7] Università di Napoli Federico II, Napoli, Italy
[8] Università degli Studi di Milano-Bicocca, Milano, Italy

E-mail: Gustavo.Granucci@istp.cnr.it

Received 15 February 2024, revised 2 July 2024
Accepted for publication 4 September 2024
Published 10 October 2024

Abstract
The Divertor Tokamak Test (DTT) facility is equipped with auxiliary heating systems in order to be able to load the divertor with a power flux relevant to study the power exhaust issue in a reactor relevant range of parameter. The powerful system is the Electron Cyclotron Heating (ECH) with an installed power of 32 MW in its largest extension. Together with the bulk heating of the DTT plasma, the ECH system will cover several tasks for the plasma operation. This paper summarizes the main characteristics and design choices of the DTT ECH system and the related physics studies, based on the reference DTT plasma, to develop and control the plasma, fulfilling the functional tasks, with the support of simulation activities. Dedicated studies have been carried out to investigate the capability of EC power to assist plasma start-up, stabilize MHD activity and support current ramp up/down. In addition, it has been studied how changes of the ECH power distribution can have an impact on the plasma profiles, affecting the fueling pellet effectiveness and MHD modes.

Keywords: tokamak, heating system, ECRH

(Some figures may appear in colour only in the online journal)

---

[*] Author to whom any correspondence should be addressed.

1. Introduction

The aim of Divertor Tokamak Test facility (DTT) [1] is to study, in an integrated way, a solution for the power exhaust in conditions relevant for DEMO. To accomplish this task, DTT will require the deposition of about 45 MW of additional power to the plasma. The main characteristics of DTT facility are summarized in table 1. The additional heating systems [2] chosen to achieve this goal are the Electron Cyclotron Heating (ECH), Ion Cyclotron Heating (ICH) and Neutral Beam Injector (NBI). The total installed power of 50 MW will be made available incrementally in 3 different phases: 8 MW of ECH will be at hand for the first plasma (2 MA, 3 T), to which further 8 MW of ECH and 4 MW of ICH will be added to complete the first phase. In the second phase, 10 MW of negative NBI (at 510 keV) will be installed. In the final third phase, both ECH and ICH power will be doubled, leading to the target of 45 MW to be injected into the DTT plasma, considering the losses in the transmission lines and the coupling systems. The technical description of the three DTT heating systems are described in [3–5], where these results in term of transmission efficiency are reported. The injected power, by these three systems, has a relevant fraction of direct electron heating considering the amount of power (more than 28 MW) by ECH, which is a one of the larger amounts between every existing tokamaks and second only to the one envisaged for ITER.

The ECH DTT system is designed in a modular way, with the novelty of an evacuated multibeam Quasi Optical (QO) Transmission Line (TL) connected to individual front-steering launchers with the highest flexibility. Moreover, with the current available gyrotron unit power of 1 MW at 170 GHz, up to 32 gyrotrons will be installed and operated simultaneously, making DTT closer to DEMO for its relevance and complexity. Several tasks will rely on the ECH capability for localized plasma heating and current drive, including the need for a flexible and fast actuator to be used in control loops, a key feature of future fusion reactors. The paper is organized in the following way: in the second section the ECH system is described with the list of the major tasks expected from it and with the details on the launcher capabilities; in the third section the results on simulations for the EC assisted breakdown in DTT are presented; in the fourth the needs for the MHD control; in the fifth the results on simulation related to the bulk heating and the effect of propagation in high density plasma; in the last two paragraph the role of ECH in the control of plasma current ramp up and ramp down are reported. At the end the conclusions.

2. The DTT ECH system

Table 1. DTT main parameters.

Major radius (m)/Minor radius (m)	2.19/0.7
Toroidal magnetic field (T)	5.85
Plasma current (MA)	5.5
Additional heating power injected (MW)	45
Pulse length (s)	100
First wall/Divertor material	Tungsten

The system's development strategy places a strong emphasis on achieving high reliability, promoting a modular architecture and minimizing maintenance requirements. It prioritizes the use of proven and evaluated technologies to meet the schedule and to avoid risk in procurement strategy. A dedicated building for ECH will be constructed as close as possible to the DTT hall, ensuring that it remains within the tolerable range of the external magnetic field, generated by the tokamak, to guarantee the gyrotrons operations. Based on the different phases of power required, the system has been organized in 4 clusters. Each of them is composed by 8 gyrotrons, fed in pairs by four main high voltage power supplies and connected to the DTT tokamak with one evacuated QO single/multi beam TL and 2 launching antennas in the same vacuum vessel sector: one located in the equatorial port and the other in the upper port. The ECH system layout in its full configuration, including all the related equipment, is shown in figure 1-left with the ECH dedicated building connected to the Tokamak Hall through a bridge where the multi-beam TLs will be installed.

The source requirements are largely based on the ITER gyrotron parameters and for this reason the procurement has been shared with the Fusion for Energy agency, arriving to an open and international tender in which Thales was selected as gyrotron supplier for DTT. The output power is 1 MW power at 170 GHz for 100 s with an efficiency larger than 40%. The manufacturing of the first Gyrotron pre-series tube has been completed by Thales and the tube (figure 1-right) is installed European test facility FALCON of the Swiss Plasma Center (SPC) in Lausanne, Switzerland [6] to perform conditioning, long pulse test and the final acceptance test. The results of the preliminary tests have shown the compliance with the main technical requirements in terms of power output, frequency and efficiency. Based on this, the contract for the manufacturing of the following 15 Gyrotrons has been signed and the related activities started. The goal is to install 8 Gyrotrons for the first plasma operation, completing the supply for the first DTT phase. The TL concept is based on the fully quasi-optical propagation of up to 8 Gaussian beams, similar to solution adopted in Wendelstein 7-X [7], but under vacuum to strongly reduce the risk of arcing. The propagation in the main section takes place with large mirrors dedicated to the bundle of 8 beams, in a Gaussian beam telescopic arrangement of alternating plane and focusing mirrors to recover the unavoidable beam distortions due to the off-axis reflections. The mm-wave system is designed to give TL losses below 7%, considering ohmic and spillover losses only [3]. The ECH power is employed throughout the plasma discharge to perform different tasks. Some of the main functions, arising from the physics simulation of the different DTT scenarios, are reported in table 2.

The 8 beams bundle of each cluster is split, before to enter in the ECH antennas: 6 beams into the equatorial antenna (organized into 2 rows of 3 modules) and 2 beams in the upper one. The four DTT-ECH equatorial antennas of the whole

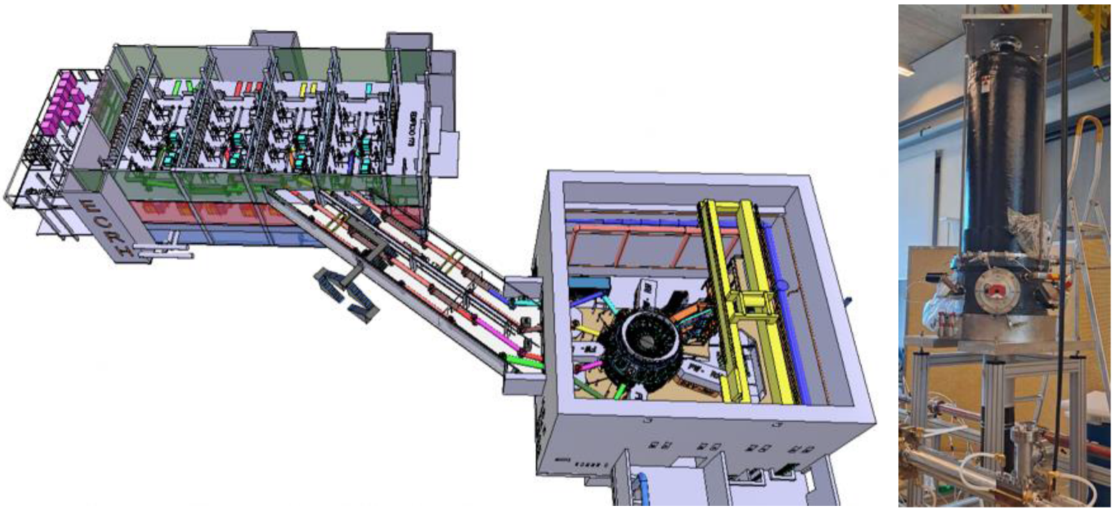

Figure 1. Left: Layout of the DTT-ECH system in the full configuration and overview of the ECH building connected to the Tokamak Hall; Right: DTT Gyrotron pre-series at Falcon Test Facility for FAT (THALES property and confidential information, not to be disclosed).

Table 2. DTT-ECH system tasks.

Plasma discharge phase	Targeted physics functions
Start-up	Improve pre-ionization to initiate plasma Save transformer flux consumption to increase plasma duration
Ramp-up	Save transformer flux consumption by reducing plasma resistivity Helps to build up temperature and current Tailors current profile for stabilizing plasma Early transition L-mode to H-mode
Flat top	Tailoring current/temperature profile Controls of sawteeth and NTMs Sustain H-mode Current drive to sustain flat-top duration Avoid impurity accumulation Diagnostics application (i.e. Collective Thomson Scattering)
Ramp-down	Sustain temperature during H- to L-mode transition Control current profile to avoid instabilities
Plasma restart operation	Wall cleaning

system are dedicated manly to plasma heating and current drive (CD) while the four upper antennas to the stabilization of MHD instabilities. A single launching module unit, consisting of a stainless-steel waveguide section, a fixed focusing mirror (M1) and a plane front-steering mirror (M2), all water-cooled is dedicated to each beam line, giving the highest possible modularity and flexibility in terms of power distribution over all the entire minor radius. The present layout of the equatorial antenna design is reported in figure 2 (left), evidencing the compact integration as result of the maximization of the injected power per port.

As no window is foreseen between the TL and the torus vessel, the introduction of a section of waveguides (63.5 mm i.d.) is necessary to reduce the vacuum conductance between the evacuated environment of the TL and the tokamak. The two vacuums are connected only during the plasma discharge, being the connection managed by all-metal gate valves.

The mirrors will be realized by exploiting the additive manufacturing technique. To this aim a first prototype of the fixed mirror M1 in CuCrZr has been manufactured, with a spiral cooling channel capable to sustain a peak loading up to 1.68 MW m^{-2}. A picture of the mirror at the end of the printing process is shown in figure 2 (right). Once the final finishing of the mirror, it will be subject to high power tests at the FALCON test facility to assess this manufacturing solution.

The design of the launchers has been done in order to cover, with the launched beams, the largest part of the plasma section, and assuring a good current drive efficiency for all the foreseen scenarios. Even if a large fraction of EC Current Drive (ECCD) is not a specific requirement of the ECH system of DTT, this capability represent a potentiality for future applications, that could be of great interest in the DTT Research Plan [8]. Examples of the beam paths launched from the upper and from the equatorial port launcher positions are shown in

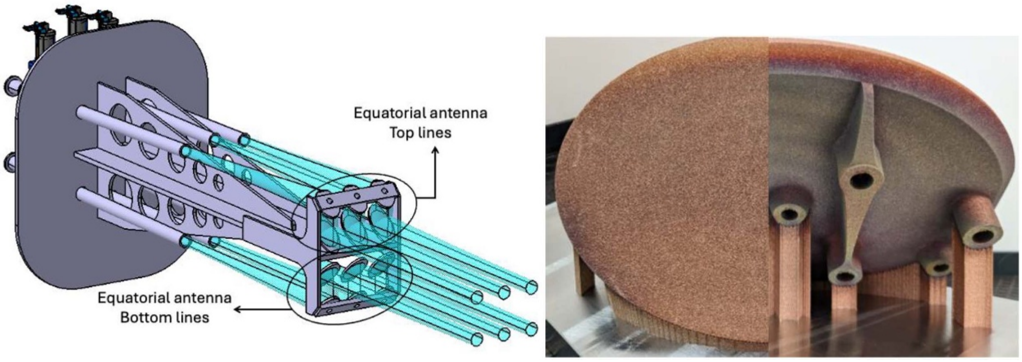

Figure 2. Left: Equatorial antenna design made of 6 launcher module units (3 top lines + 3 bottom lines) with supporting structure. Cyan surfaces represent the Gaussian beam propagation after the in-vessel waveguide termination up to the plasma; Right: front and rear views of the prototypes in additive manufacturing of the fixed mirror M1 of the launching module.

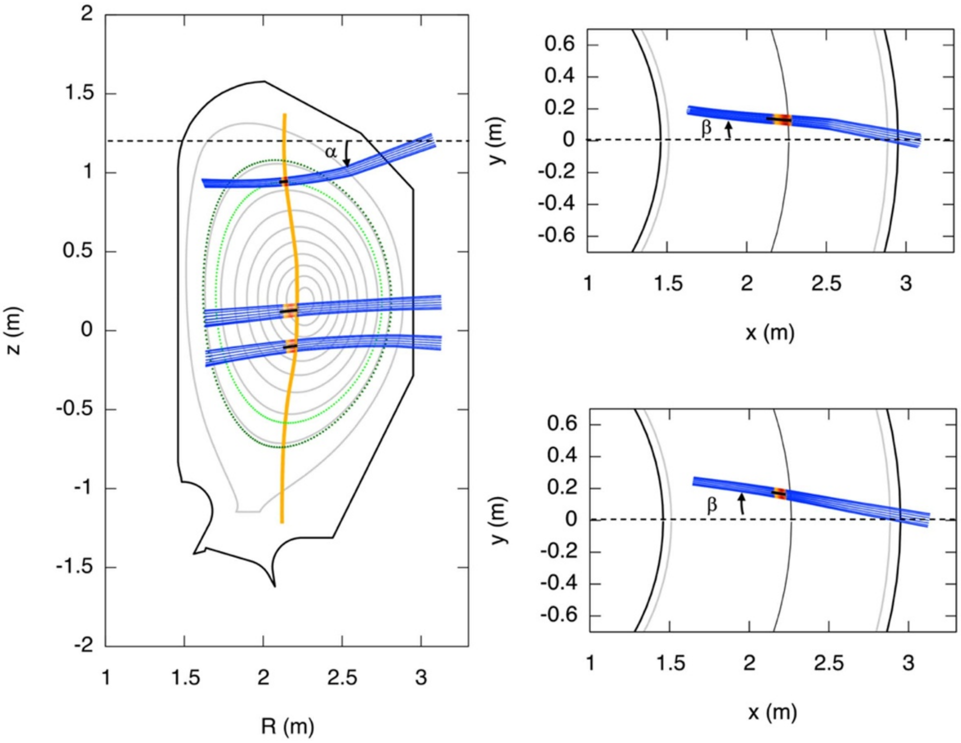

Figure 3. Poloidal (left) and toroidal (right) projections of the flux surfaces of the reference full power scenario and of the path of different EC beams varying the launching position/angles (O-mode polarization). In yellow the resonance layer for 170 GHz. In (dark) green the poloidal projection of the $q = 3/2$ ($q = 2/1$) surface. The poloidal (α) and toroidal (β) injection angles are indicated in the figures. The EC beam shown in the toroidal projection on top-right is launched from the upper antenna and on bottom-right from equatorial one.

figure 3, which represents the poloidal and toroidal sections of the flux surfaces of the plasma foreseen for the reference scenario. To fulfill the tasks assigned to ECH system the front steering mirrors have been designed with the widest possible flexibility, with real time controllable mirrors with an angular speed of 20°/s that means a $\Delta\rho_t/\mathrm{d}t$ of 0.6/s (where ρ is defined as normalized toroidal radius, calculated as the squared root of the normalized toroidal flux) in order to be able to quickly follow the request coming from the control system. Details on steering capability are reported in figure 4. The launching steering range are defined in the table of figure 4 (left), where α and β are the poloidal and toroidal launching directions while θ and ϕ are the correspondent mechanical angles. The ECH launcher performance in terms of driven current density distribution and reachable position are shown in figure 4 (right) respectively for the three modules in the equatorial antenna (top and bottom region), and the two modules of the upper antenna. The beam radii at the plasma resonance are respectively 44.5 mm and 15 mm for the equatorial and upper antenna.

<table>
<tr><th colspan="2">Equatorial Top</th><th colspan="2">Equatorial Bottom</th></tr>
<tr><td>α</td><td>β</td><td>α</td><td>β</td></tr>
<tr><td>[-25°, 10°]</td><td>±25°</td><td>[-20°, 15°]</td><td>±25°</td></tr>
<tr><td colspan="2">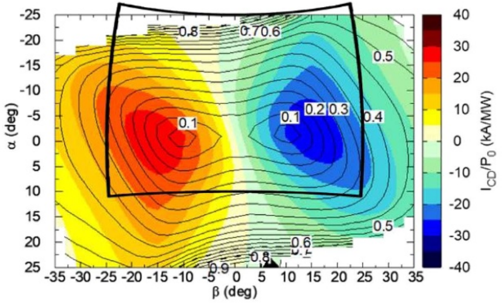
</td><td colspan="2">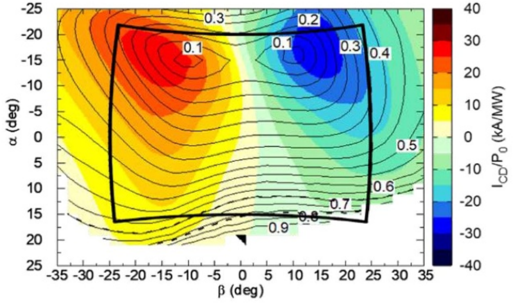
</td></tr>
</table>

<table>
<tr><th colspan="2">Upper Port</th></tr>
<tr><td>α</td><td>β</td></tr>
<tr><td>[-10°, 45°]</td><td>±22.5°</td></tr>
<tr><td colspan="2">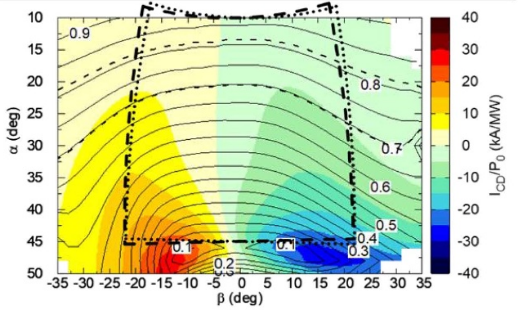
</td></tr>
</table>

Figure 4. Left: Launching angular steering range allowed by DTT first wall constrains; Right: CD efficiency maps (in color) obtained with GRAY for the DTT reference full power scenario launching O-mode polarization. Blank areas refer to couples of angles which give absorbed power in the plasma less than 90%. Solid thin black lines represent the contour of the toroidal normalized radii correspondent to the current average location. Dashed thin black lines refer to the position of the rational surfaces $q = 3/2$ and $q = 2$. Thick black curves delimit the region of the plasma reached by the launched beams, taking into account the designed wide angular capability of the front-steering mirror.

3. Assisted breakdown

The ECH power in DTT could be used to perform assisted breakdown scenario. This technique will be necessary to guarantee a robust and reliable start-up in future large superconductive devices like DTT such as ITER and DEMO, as also demonstrated very recently in JT-60SA. To prepare for different scenarios, a series of simulations were conducted employing BKD0 [9] to model the time evolution of the main plasma parameters, and CREATE-BD [10] to simulate magnetic scenario from pre-charge conditions to rump-up, and GRAY code [11] to assess the EC absorption. A coupled magnetic/kinetic scenario optimization and simulation using the three codes has been implemented through an iterative algorithm. Initially, an absolute tolerance is set for comparing plasma currents calculated by the CREATE-BD and BKD0. At the first step, given requirements in terms of electric field and stray field at BD and constraints on currents and voltages on the CS/PF coils, CREATE-BD performs an optimization of the magnetic configuration. The magnetic field map and electric field time history from CREATE-BD is then used as input for BKD0 at the second step, together with neutral pressure, impurity type and level, EC absorption tables from the GRAY code, and EC power input to determine the plasma current and the plasma resistance time history. The plasma currents are then compared, and, for subsequent iterations, which are not part of the current study, the plasma current calculated by BKD0 may contribute to further optimization or used to simulate the dynamic evolution of the magnetic quantities, maintaining the original driving voltage/currents. These codes have been already benchmarked on experimental data and exploited to study the conditions for assisted breakdown in future tokamaks. The operational conditions considered encompass two primary scenarios: a reference base line plasma at the nominal operational field at 6 T in a purely ohmic start-up with a toroidal electric field of 0.8 V m^{-1} and the operation at

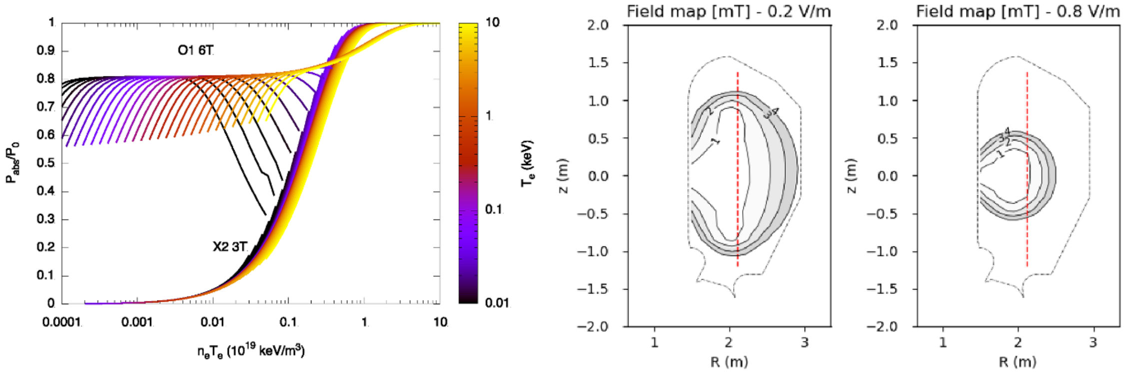

Figure 5. (left) Absorption of EC power at 170 GHz for OM1 case ($B = 6$ T) toroidally injected with an angle of 20°, and for XM2 case ($B = 3$ T), perpendicularly injected, as a function of electron density and temperature as calculated by GRAY. (right) DTT magnetic field map used for BKD0 simulation, the pre-magnetization is calculated for a toroidal electric field of 0.2 V m^{-1} and 0.8 V m^{-1}. The continuous lines are the contour levels of poloidal field at the breakdown time corresponding to 1, 2, 3, 4 mT, the vertical lines in red represents the position of the cold resonance layer for 170 GHz.

half-field, 3 T, with a conservative 0.2 V m^{-1} for systems commissioning and first plasma operation. Additionally, an EC sustained start-up at 6 T, corresponding to the ordinary mode polarization at fundamental resonance (OM1) for the 170 GHz employed in the DTT ECH system, was explored, and extended to extraordinary mode polarization at second harmonic (XM2) case at 3 T. Figure 5 illustrates the main inputs of BKD0 code used in the simulations, i.e. the power absorption calculated by GRAY at the two magnetic fields considered and magnetic conditions at the breakdown expected time, as calculated by CREATE-BD for a toroidal electric field of 0.8 V m^{-1} (plasma current ramp rate of 2 MA s^{-1}) and 0.2 V m^{-1} (1 MA s^{-1}) after 150 ms of simulation. Based on different effects of pre-ionization in OM1 and XM2, as discussed in [12] and evidenced in experimental results [13], the following different inputs are applied in BKD0 for the two polarizations injected. When ECH power is in OM, as fast and prompt breakdown is experimentally and theoretically confirmed, the electron temperature (T_e) and ionization degree are set to 5 eV and 2%, respectively. Conversely, in the case of XM2, a robust pre-ionization is needed, obtained by prolonged injection before the start of the current [14], and leading to a higher electron temperature of 200 eV (derived from [12]) with ionization degree adjusted accordingly. The parameter scan shown in figure 6 is the results of BKD0 simulations assessing the derivative of the plasma current achieved for various prefill pressures without impurities, applying a relatively small amount of ECH power, up to 3 MW of the initially available 8 MW foreseen in DTT first plasma. The plasma current rates resulting from BKD0 simulations that are reported in figure 6, represent the values to which the coupled magnetic and kinetic codes converged (2 MA s^{-1} for the high toroidal electric field and 1 MA s^{-1} for the lower ones).

The results suggest that in the ohmic scenario, the toroidal magnetic field increases the prefill pressure limit for sustained breakdown, as the stray field is maintained constant, as expected because of increasing the connection length. The limit for a sustained start-up is relatively low, ranging from 1 to 2 mPa for 0.8 V m^{-1} and less than 1 mPa for 0.2 V m^{-1} . By injecting ECH power, the toroidal electric field at 0.8 V m^{-1} provides access to prefill pressure up to 10 mPa. The operational window expands of a factor 4 for both the OM and XM modes. When the electric field is 0.2 V m^{-1}, the rise is moderate for each MW injected, with a rate of 2 mPa/MW, exhibiting a different minimum threshold (0.25 MW for OM and 1.25 for XM). Such an operative window should ensure successful breakdown also in case of impurities. A more detailed study is planned, delving into various impurity mixtures and different levels of field null dimensions and stray fields. The large availability of ECH power and its flexibility ensure in any case the possibility to have a stable and reliable sustained plasma start-up in DTT. From a magnetic point of view, a magnetic control with the actual voltage limits can support a large variety of scenarios. The availability of tools to automatically optimize the time evolution of magnetic fields [15] allows the design and testing of alternative field null configuration breakdowns but also Trapped Particles Configurations recently tested in tokamaks [16].

4. Neoclassical tearing modes control in full power scenario

A key issue to assess the plasma performances is the study of dangerous resistive helical instabilities, as the tearing modes, limiting the operations up to possible disruptive events. The dynamics of these modes, evolving as magnetic island, is modelled for both the Tearing Mode (TM), driven by the current density gradient, and the Neoclassical Tearing Mode (NTM), driven by seeded magnetic perturbations created for example at the crash of large sawtooth (ST) periods [17]. Predictive evolutions of these modes are carried out for the DTT scenarios with ST activity at 5.5 MA and 5.85 T and 21 MW power EC deposition in the core from equatorial launchers. EC power from the upper launcher up to 7.2 MW has been considered for the mode stabilization. The ST amplitude and frequency are

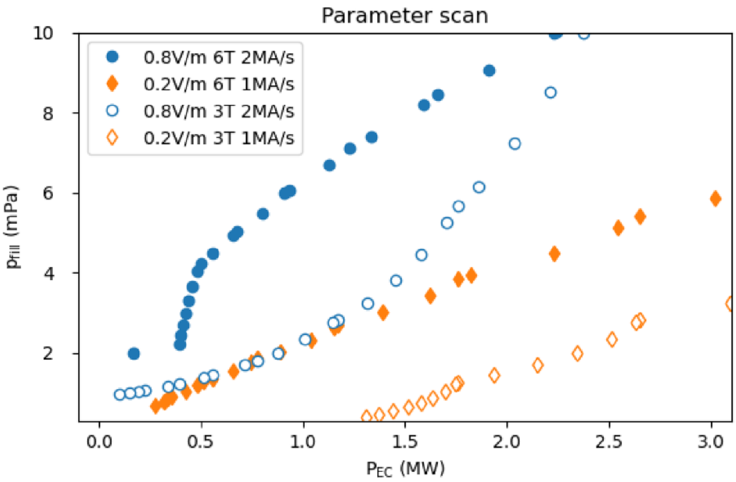

Figure 6. Parameter scan calculated with BKD0, CREATE-BD and GRAY coupled simulations. Full and empty symbols correspond, respectively, to a magnetic field of 6 T and 3 T for the different plasma current ramp rates reached in 150 ms of simulation.

calculated using the Kadomtsev complete reconnection [18] and the Porcelli trigger [19] models integrated in JINTRAC code [20]. As an important 1 Hz ST activity, corresponding to a period of 0.98 s, is found due to the $q = 1$ radius larger than the half of plasma minor radius, NTM could be triggered at the ST crash. The presence of unstable TM could be foreseen as well evolving neoclassically in size up to values larger than the critical width of NTM. The evolution and stabilization of these resistive helical unstable perturbations have been simulated using the NTM module [21] integrated in the JETTO-JINTRAC code considering destabilizing positive values of the tearing stability parameter Δ'_0 for the TM onset ($\Delta'_0 > 0$) and stabilizing negative values for the NTM one ($\Delta'_0 < 0$).

As these modes evolving to large sizes can lead to a plasma confinement degradation up to disruptions, the control of their amplitude up to the complete suppression can been studied by using a local current driven by external power sources to replace the loss of bootstrap current. To achieve this goal ECCD is used to generate local current driven in co-current direction. The upper launchers, dedicated in DTT to MHD control, can be used to deliver up to 7.2 MW, with good current drive efficiency, at the resonant surfaces where the main low order modes 3/2 and 2/1 are located. EC power can be used in un-phased (labelled as CW injection in following figures) or 50% phased inside the island aligned to its center (labelled as modulated injection) control mode, to reduce the tearing mode island amplitude and stabilize them at a full suppression of their size w ($w = 0$). In the latter case, modulation is synchronized with the rotational frequency of the NTM/TM, thus activating EC power injection when the island's O-point crosses the deposition zone. The considered injection timing follows a fixed pattern, with the EC power modulated from 0% to 100% with a duty cycle of 50%. Anyway, the control system is designed to adjust the pulse length in real time, allowing synchronization up to 5 kHz with a duty cycle from 10% to 90%. Particularly, from the simulations, reduced ECH power is generally needed with phased injection (modulated) with respect to the unphased case (CW) for island size w much smaller than EC deposition width w_{cd}. Otherwise, for $w \leqslant w_{\mathrm{cd}}$ and $w > w_{\mathrm{cd}}$ CW and modulated cases not significantly differ as shown below in figures 7 and 8. From the simulation the 2/1 stabilization requires about 4–6 kHz, while for 3/2 about 8–12 kHz. Due to the imitation in frequency of power modulation (due to the control system and gyrotron power supplies limitations) the two analyses strategies (mod or CW) will be applied whenever possible.

Time evolution and suppression for the full power scenario of the 2/1 and 3/2 NTM and TM has been simulated and the results reported in figures 7 and 8. In this scenario both the modes are located off-axis at $\rho_{2/1} = 0.82$ and $\rho_{3/2} = 0.72$ of the normalized toroidal minor radius. The beams used in the simulation are launched from upper antenna (see figure 3). Both the 2/1 and 3/2 parameters stability are $r_{\mathrm{s}}\ \Delta'_0 = 0.1$ for TM and $r_{\mathrm{s}}\ \Delta'_0 = -1$ for NTM. The destabilizing Δ'_{bs} term originated by the perturbed bootstrap current of the 3/2 NTM is 30% larger than the 2/1 NTM one.

Assuming a minimum island width of 0.02–0.04 m for the mode detection, different amount of EC power is required for stabilization if it is switched ON when, for example, the mode size reaches 0.021–0.023 m or 0.04 m. In figure 7 (left) the time evolution without and with ECCD of the 2/1 TM, triggered at 40.7 s, are shown with the electron temperature on axis (T_{e}, ax) as well. The values of the power needed for the mode full suppression are indicated for the phased (mod) and unphased (CW) injection. The ECCD is 1.4 kA/MW with a current density width of $w_{\mathrm{cd}} = 0.0256$ m. The mode is suppressed in 0.25 s with only 4 MW of modulated power if injected at $t = 40.72$ s when the mode width is 0.023 m, while 6 MW are required if injected at $t = 40.85$ s when the mode size is 0.04 m. In this latter case modulated power full stabilizes the mode in 0.650 s while the CW injection in 0.950 s. In figure 7 (right) same kind of evolutions are shown for the NTM triggered by the sawtooth crash at 40.66 s. This mode is suppressed with 1.5 MW, switched ON at 40.85 s when the

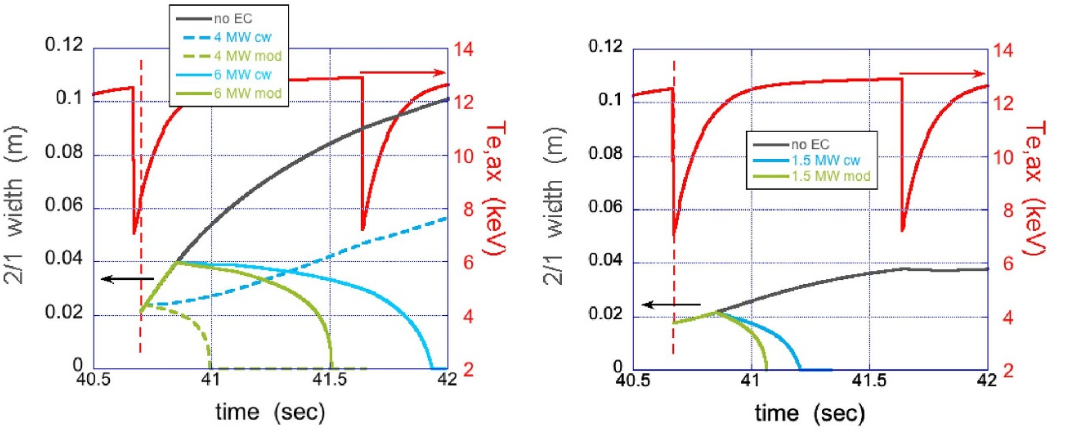

Figure 7. Sawtooth period (continuous red line) and 2/1 TM (left) and NTM (right) width evolution without EC power injection (continuous gray line), at different EC power in CW (blue lines) and modulated (green lines). Vertical dashed lines indicate the onset of the modes: TM at 40.7 s and NTM due to sawtooth crash at 40.67 s.

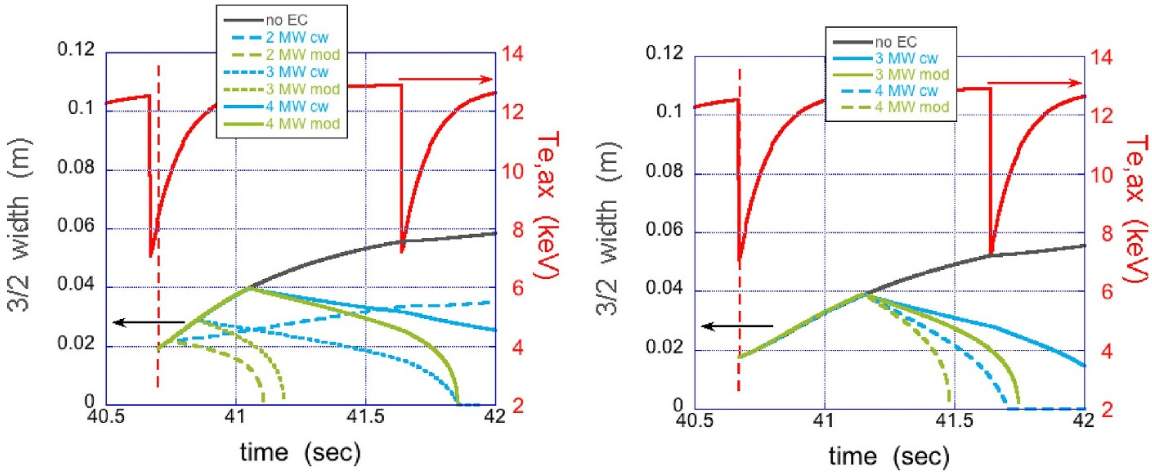

Figure 8. As figure 7 for 3/2 mode. Sawtooth period (continuous red line) and 3/2 TM (left) and NTM (right) width evolution without EC power injection (continuous gray line), at different EC power in CW (blue lines) and modulated (green lines).

mode width is 0.021 m, in 0.215 s by modulated injection and in 0.35 s by CW power.

Figure 8 as figure 7 for the 3/2 TM (left) with the time evolution of T_e on axis and of the 3/2 width evolution without and with ECCD power. In this case driven current is 3 kA/MW, due to the inner deposition while the current density deposition width is $w_{cd} = 0.0343$ m. The mode stabilization is studied by injecting power at three different time corresponding at three different mode widths: $w = 0.0213$ m at $t = 40.7$ s, $w = 0.028$ m at $t = 40.85$ s and $w = 0.04$ m at $t = 41.05$ s. In the first case the control is obtained in 0.36 s with 2 MW EC of modulated injection only, while in the second case 3 MW are needed for the suppression obtained in 1 s and 0.35 s with CW and modulated power respectively. In the latter case the mode is stabilized with 4 MW in 1.55 s and 0.81 s with CW and modulated power respectively. In figure 8 (right) same evolutions are shown for the NTM. This mode can be suppressed with 3 or 4 MW applied at 41.15 s when the mode size is 0.04 m. The control is obtained with 3 MW in 1 s and 0.81 s with CW and modulated power respectively and with 4 MW in 0.55 s and 0.33 s with CW and modulated power respectively.

As expected, the simulations show that using the same amount of CW and modulated power when $w \leqslant w_{cd}$ and $w > w_{cd}$ the full control of the TM and NTM can be obtained, but in different times, longer with CW of about 0.2–0.3 s. In any case, a control done up to 1.4 s can be considered reasonable. These results highlight that a limited amount of CW power can be sufficient for the mode control avoiding the intrinsic limitation introduced by hardware in modulating high level of power. In addition, it should be noted that a further reduction of EC power needed to mode control can be obtained taking into account also the heating effect on the stabilization, not considered in these first analysis. The misalignment of the power deposition with respect the mode localization has not be investigated as well to quantify on the contrary how much more power could be necessary for the stabilization. In our present results an ideal power absorption in the center of island has been considered. These results will be used as input to the

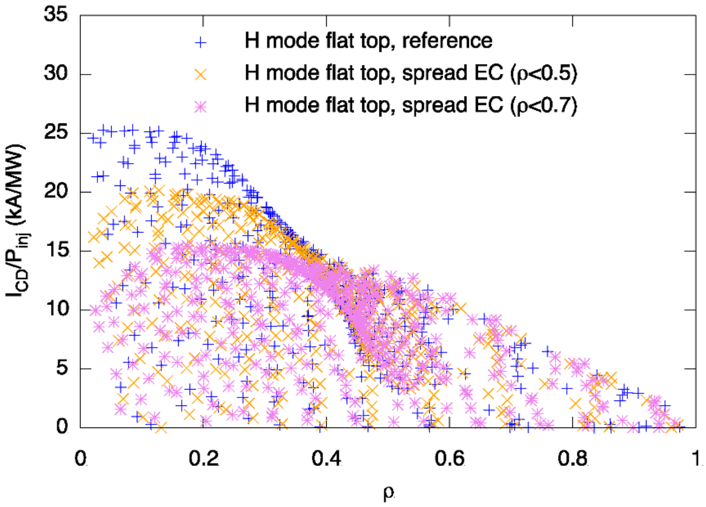

Figure 9. Calculated driven current per unit power dependent on driven current average location for the equatorial top launcher. Each point corresponds to a different set of injection angles. For the represented points complete EC power absorption is obtained. Blue: the reference flat-top with central peaked EC deposition; orange: flat-top with spreader EC deposition ($\rho < 0.5$); violet: flat-top with extremely spread EC deposition and peaked density profile ($f_{GW} \sim 0.6$) ($\rho < 0.7$).

design of the stabilizing control system, in term of diagnostic capability, intervention speed and overall strategy.

5. Bulk heating and current drive in full power scenario

In order to investigate and to optimize the EC performances, parametric studies have been performed considering the updated DTT full power scenario, consistently calculated with the last version of the DTT antenna design, which is characterized by an upward vertical plasma shift of 12–13 cm [22]. Two options are currently under study: the reference scenario, with central peaked EC power deposition, and a second one, with broader EC power deposition, needed to sustain the core plasma density using pellet injection as fueling method [23]. The investigation has been carried out with the beam tracing code GRAY, varying the toroidal and poloidal injection angles, launching OM1 and considering the EC launcher specifications as described in section 2. Complete absorption is found for large angles intervals, while engineering constraints give narrower limits (see figure 4 right) [24]. The allowed ranges of angles permit to reach the plasma in the central region ($\rho \sim 0.1$) as the peripheral core plasma ($\rho < \sim 0.7$–0.8) from every launcher position. The maximum current is driven in correspondence of $\rho \sim 0.1$, with a value of ~25 kA/MW for the reference scenario (see figure 8). Slightly lower central driven current is found for the case of broader EC power deposition. Scenarios characterized by higher Greenwald density fraction ($f_{GW} \sim 0.6$) than the reference full power scenario ($f_{GW} \sim 0.4$) have been investigated considering largely spread EC power deposition profiles [23]. Peaked density profiles decrease the values of the driven current in the central plasma region. The OM1 EC cut-off density, which is $\sim 3.5\ 10^{20}\ \mathrm{m}^{-3}$, is not achieved, then the EC beams can reach the plasma center with complete absorption. However, high Greenwald density fraction plasmas are planned to be studied in DTT with lower plasma current values and with densities well below the EC cut-off density.

The EC performance investigation has been carried out considering different levels of impurities, recovering the expected dependence of the EC driven current efficiency on $1/(1 + Z_{\mathrm{eff}}/5)$ (see figure 9). Core heating and CD are well performed for the two scenario options, then allowing the accomplishment of the task of bulk heating. Such considerations refer to the flat top phase of the full power scenario. In addition, a preliminary investigation has been performed at the end of the ramp up phase. As shown in figure 10 the driven current is significantly lower with respect to the flat top phase only in the plasma center, while for $\rho > 0.2$ the I_{cd} values obtained with the same Z_{eff} are comparable for the two phases of the discharge.

Furthermore, with varying the injection angles, a large interval of radial locations is reached, allowing both on and off axis deposition. Numerical studies regarding the EC performance during the ramp up phase are ongoing. The impact of the perturbation due to the pellet deposition on beam propagation has been investigated for the DTT full power scenario, assessing the ECH performance in time-dependent scenarios with pellet injection. First studies with the stand-alone version of GRAY have been performed [25]. The inner plasma core is always reached by the EC beams without any noticeable deviation. In the region of the rational surfaces a maximum poloidal angle correction of few degrees is required by the radial deviation of the power localization with respect to the case without pellet profiles. However, no corrections are required if the density profiles corresponding to the initial and final time of a pellet cycle are considered. Then the interaction between the beam propagation and the density deviation due to pellet injection has been investigated by integrated simulations [26]:

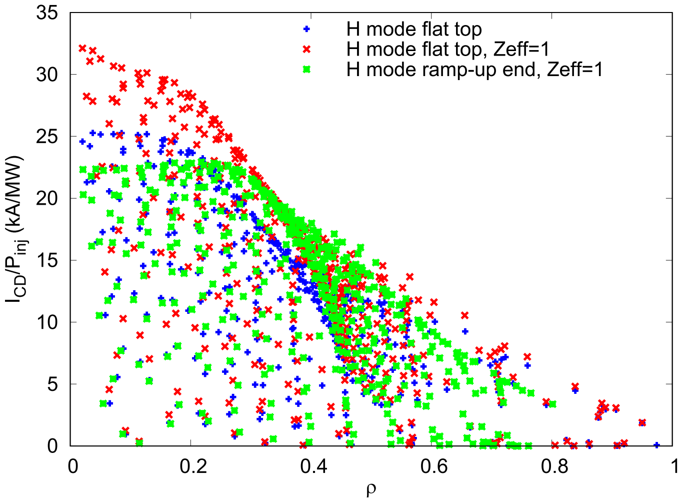

Figure 10. Calculated driven current per unit power dependent on driven current average location for the equatorial top launcher. Each point corresponds to a different set of injection angles. For the represented points complete EC power absorption is obtained. Blue: the reference flat-top with $Z_{\mathrm{eff}} = 1.7$; red: flat-top with $Z_{\mathrm{eff}} = 1$; green: end of ramp-up (lower T_{e} peaking) with $Z_{\mathrm{eff}} = 1$.

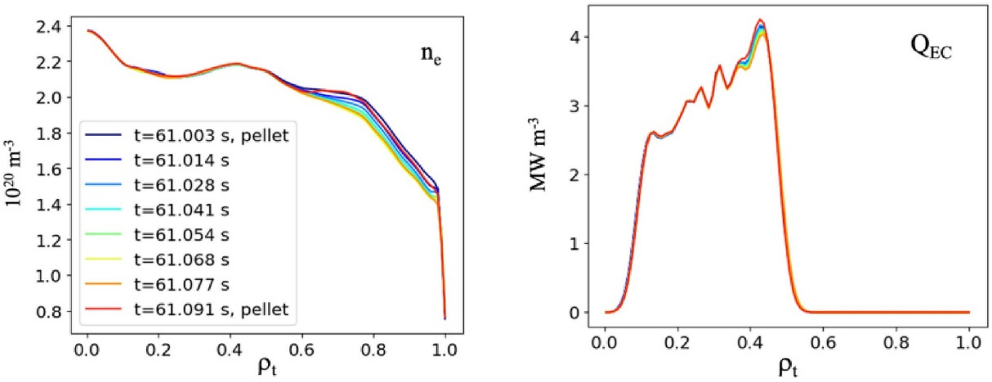

Figure 11. Left: Electron density profiles by the simulations of the DTT full power scenario with transport model QuaLiKiz. The temporal slices of the density profile during a pellet cycle relative to the self-consistent calculation of the EC deposition are represented. Right: the relative GRAY self-consistently calculated EC power deposition profile.

the code GRAY and the code HPI2 [27] for the pellet ablation/deposition calculation have been used self-consistently in the transport code JETTO, with the simplified gyrokinetic transport model QuaLiKiz [28] for heat and particle transport predictions.

The EC power deposition is negligibly modified by refraction changes both during a single pellet cycle and after several pellet cycles, indicating full compatibility between the EC launching system and the pellet injection system (see figure 11). The presented estimates of the ECCD performances do not take into account any eventual impact of EC beam broadening on the deposition profiles. It can be caused by the beam scattering off the turbulent density structures proper to the edge region of the plasma. Experimental works and theoretical and modelling studies indicate that this effect is significant for large machines as DIII-D [29], and it could be substantial for reactor-sized fusion machines like ITER [30, 31]. In smaller devices like DTT, which are usually characterized by superdiffusive beam broadening regime, such phenomenon seems to marginally affect the EC deposition profiles [31, 32]. However, recent studies highlighted the role that the launching configuration can have in the impact of the edge turbulence on the deposition profile broadening also for tokamaks with small dimensions [32]. A predictive study including the edge turbulence regime foreseen for DTT could be interesting to individuate recommended launching configurations with acceptable broadening. However, the low order of magnitude of the deposition broadening as foreseen for small devices, together with the uncertainty given by the assumptions on the edge turbulence, could give ambiguous results. Validated extrapolations for the characteristics of the edge turbulence and better understanding of the phenomena which give deposition broadening in small machines are needed [32].

6. Current ramp-up

The DTT scenario E-SN has been simulated by means of the METIS code, a fast numerical tool able to explore a wide range of parameters [28]. The code receives a wide set of numerical

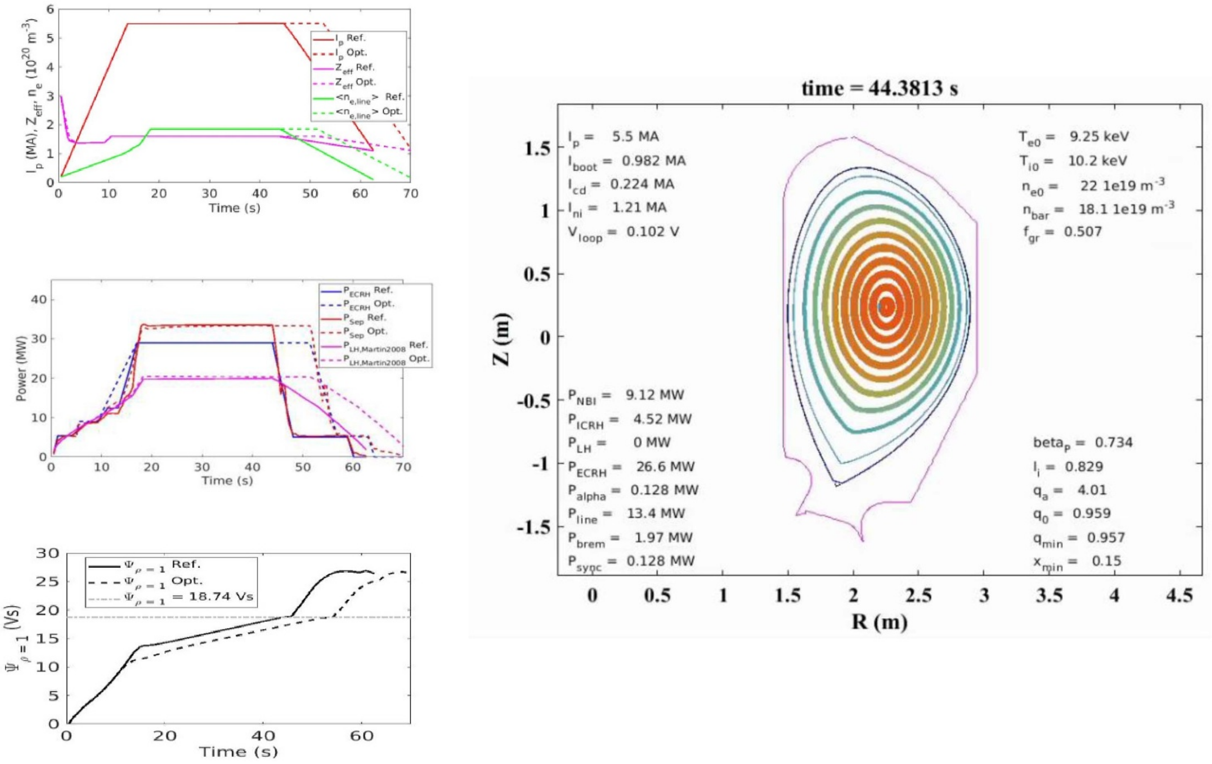

Figure 12. METIS scenario of the DTT E-SN scenario (full field, full current, full power). Time evolution of I_p, $<n_{e,line}>$ and Z_{eff} (top left); time evolution of the additional ECH power, of the power crossing the separatrix P_{SEP} and the LH power threshold P_{LH} (center left); consumed (black) and available (gray) magnetic flux $\Psi = 18.74$ Vs (bottom left); magnetic equilibrium at the end of flat top phase (right). The reference and the optimized scenario are shown with solid and dashed line, respectively.

parameters to define the plasma conditions and the scenario. The user can act on the waveform of several quantities, as the external power (NBI, ECH, ICH) and the line average density, to optimize the discharge by taking into account the main limiting factor, such as the electromagnetic controllability or the available magnetic flux. The main plasma parameters of the scenario refer to [33]. The modelled METIS reference scenario is shown in figure 12 with solid lines in terms of time evolution of the current, density, Z_{eff}, ECH. The NBI and ICH (not shown here) also contribute to the total heating power mix during the flat top phase. The magnetic equilibrium at the end of the flat top phase is also shown. The scenario is characterized by a current ramp up rate of 400 kA s^{-1} and a total available magnetic flux of $\Delta\Psi = 18.74$ Vs at the end of the flat top. The latter estimate is obtained by considering a real premagnetization of 16.2 Vs and a flux consumption in the breakdown phase without ECH of $\Delta\Psi = 1.55$ Vs [34]. An extrinsic Ne seeding is considered in the simulation with $Z_{\mathrm{eff}} = 1.6$, to be consistent with the typical SOL operational conditions in detached divertor plasma as predicted by SOL modelling [35, 36]. Also, W is taken into account with a mean impurity density ratio $n_{\mathrm{W}}/n_{\mathrm{Ne}} = 0.004$. The corresponding total radiated power inside the core is $P_{\mathrm{rad}} \approx 15$ MW.

The constraint on the available magnetic flux strongly limits the flat-top and discharge duration. In the reference case, where the L-H transition occurs at $t \approx 15$ s, the flat top phase lasts for $\Delta t = 26$ s. The ECH is used during the ramp-up phase but with the strict limit that the power crossing the separatrix must be lower than P_{LH} (evaluated with 2008 Martin scaling [37]). In order to optimize the magnetic flux consumption, the EC power waveform has been optimized to extend the achievable flat-top discharge duration. A faster ECH ramp up rate has been defined during the ramp-up phase of the discharge. As a result, a reduction of the plasma temperature and of the resistivity is obtained which yield, in turn, to a strong reduction of the resistive consumed magnetic flux. The optimized scenario is depicted with dashed line in figure 12. An increase in the discharge duration by $\Delta t = 8$ s is obtained. However, an early LH transition at $t \approx 10$ s may occur. These results can be used as a starting point of more sophisticated analyses. In particular, further investigations are needed to assess the stability and the feasibility of the optimized scenario.

During the ramp-up phase, another critical point is necessity to counteract the current density peaking leading to the MHD instability. This behavior can be assessed through the evolution of the parameter l_{i} and can be mitigated by acting on the EC deposition profile with an off-axis deposition [38]. Figure 13 shows two different situations: the EC power deposited either totally off-axis, set with a Gaussian centered on $\rho = 0.6$, or with a deposition both off-axis (on $\rho = 0.6$) and on-axis (on $\rho = 0.22$). The former case is commonly adopted in METIS for a first estimate by assigning the position of the maximum deposition, while the latter shape has been defined by referring to the ASTRA (shown in orange) time dependent ramp-up modelling [34]. The results in terms of β_{p} are close in the two cases because of the same total EC power.

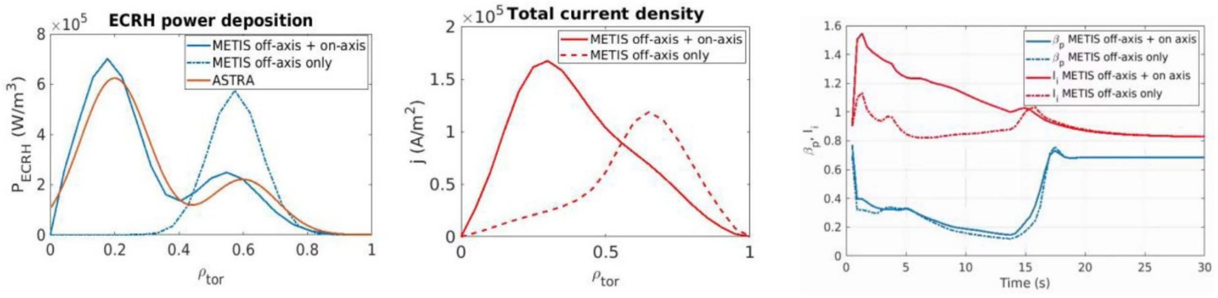

Figure 13. ECH power deposition profile during the ramp-up phase of the DTT SN scenario (left); total current density profile (center); and the corresponding values of l_i and β_p obtained in METIS. P_{ECH} and j profiles are taken at t = 4 s.

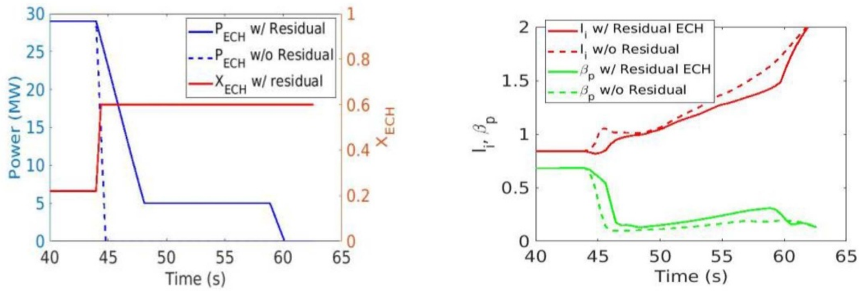

Figure 14. Left: Time evolution of the ECH power (blue) and maximum deposition location (red) in the ramp-down phase of the DTT SN scenario. Right: Results in terms of internal l_i and β_p obtained in METIS. The label 'Residual' refers to a residual ECH power retained during the ramp down phase.

The two P_{ECH} deposition profiles reflect in a different current density, with the mixed on-axis and off-axis deposition resulting in more peaked j profile. For instance, the resulting j profiles at $t = 4$ s is shown, together with the corresponding P_{ECH} profile. As a result, the EC deposition strongly affects the l_i evolution, especially in the first phase of the discharge: if on-axis deposition is present, l_i sharply increases at the beginning, when the plasma is still in limiter configuration ($t < 5$ s), and then decreases to the same values at the L-H transition ($t > 18$ s) whilst in case of off-axis only the l_i value is kept below one throughout the ramp-up phase. However, a slight effect is observed on the resistive flux consumption with an increase of 10% for the off-axis only case, thus reducing the available magnetic flux and shortening the flat top duration. In addition, a central ECH power deposition is beneficial in terms of tungsten accumulation, as discussed in [39]. Therefore, the best choice comes from a compromise between EM controllability and flat-top duration.

7. Current ramp-down

The current density peaking and the consequent increase in l_i is also observed during the ramp-down of the discharge. Figure 14 shows the time evolution of the ECH power and the corresponding METIS results in terms of l_i and β_p in ramp-down phase of the DTT E-SN scenario with (solid) and without (dashed) the use of a residual EC power of $P = 5$ MW. The current density tends to peak with a direct effect on l_i that suddenly increase to 1 at the end of the flat top ($t = 46$ s) when the plasma is still in X-point configuration, thus compromising the plasma controllability. The use of a residual EC power with an off-axis deposition (at $\rho = 0.6$) is able to counteract the current peaking during the ramp down. The l_i values tend to increase slowly and to be below 1.2 for most of the ramp-down duration. The increase in the last part of the discharge is of minor concern since we have a small plasma in limiter configuration.

8. Conclusion

This work presents the design choices and the investigations on the physics capabilities of the DTT-ECH system, whose dimension and power availability are comparable to those of ITER and DEMO. This heating system allows to anticipate issues for reactor class tokamaks and, thus, to solve common problems. The design of the ECH DTT system is characterized by a strong modularity and a full flexibility in the power steering and deposition control in the plasma. In the DTT scenarios, several applications of the ECH power have been studied beyond the bulk heating, as the assisted startup (to guarantee a wide operation window in terms of toroidal electric field and prefilling pressure) or the current tailoring during the ramp-up. In fact, an off-axis heating is necessary to control the internal inductance by widening the plasma current profile during the growth of the current. The possibility to inject relevant power at half radius is important also in the ramp down phase, when again the control of plasma current allow to avoid instabilities growth. The EC current drive obtained in DTT is also necessary in order to control MHD during the flat top phase, acting on sawteeth and NTM, one of its typical applications. A fully controllable high level ECH power is therefore necessary in the future class of tokamak, that what to confine high power during the flat top phase, as DTT that will perform these scenarios to load the divertor and study the solution to the power exhaust problem.

ORCID iDs

F. Auriemma https://orcid.org/0000-0002-1043-1563
L. Aucone https://orcid.org/0000-0003-3949-678X
B. Baiocchi https://orcid.org/0000-0002-1483-3113
A. Bruschi https://orcid.org/0000-0002-0139-6401
L. Figini https://orcid.org/0000-0002-0034-4028
P. Mantica https://orcid.org/0000-0001-5939-5244
M. Mattei https://orcid.org/0000-0001-7951-6584
A. Romano https://orcid.org/0000-0002-1228-6005
S. Schmuck https://orcid.org/0000-0003-4808-5165

References

[1] Ambrosino R. *et al* 2021 *Fusion Eng. Des.* **167** 112330
[2] Granucci G. *et al* 2017 *Fusion Eng. Des.* **122** 349–55
[3] Garavaglia S. *et al* 2021 *Fusion Eng. Des.* **168** 112678
[4] Ceccuzzi S. *et al* 2023 The ICRF Antenna of DTT: design status and perspectives *AIP Conf. Proc.* **2984** 030015
[5] Agostinetti P. *et al* 2023 *Fusion Eng. Des.* **192** 113638
[6] Goodman T.P., Cavinato M., Chavan R., Mas-Sanchez A., Santos Silva P., Vagnoni M., Tersztyanszky T. and Carre S. 2020 *IEEE Trans. Plasma Sci.* **48** 1537–42
[7] Empacher L. and Kasparek W. 2001 *IEEE Trans. Antennas Propag.* **49** 483–93
[8] Crisanti F. *et al* 2023 Physics basis for the divertor tokamak test facility *Nucl. Fusion* **64** 106040
[9] Granucci G. *et al* 2015 *Nucl. Fusion* **55** 093025
[10] Di Grazia L.E. and Mattei M. 2022 *Fusion Eng. Des.* **176** 113027
[11] Farina D. 2007 *Fusion Sci. Technol.* **52** 154
[12] Farina D. 2018 *Nucl. Fusion* **58** 066012
[13] Stober J. *et al* 2011 *Nucl. Fusion* **51** 083031
[14] Jackson G.L., deGrassie J.S., Moeller C.P. and Prater R. 2007 *Nucl. Fusion* **47** 257
[15] Mattei M. *et al* 2023 A new design tool for startup in large tokamaks with superconducting coils *29th IAEA-FEC* (*London*)
[16] An Y., Lee J., Jo J., Jung B.-K., Lee H., Chung K.-J., Na Y.-S., Hahm T.S. and Hwang Y.S. 2017 *Nucl. Fusion* **57** 016001
[17] Sauter O. *et al* 2002 *Phys. Rev. Lett.* **88** 105001
[18] Kadomtsev B.B. 1976 *Sov. J. Plasma Phys.* **2** 389
[19] Porcelli F., Boucher D. and Rosenbluth M.N. 1996 *Plasma Phys. Control. Fusion* **38** 2163
[20] Romanelli M. *et al* 2014 *Plasma Fusion Res.* **9** 3403023
[21] Sauter O., Buttery R.J., Felton R., Hender T.C. and Howell D.F. (contributors to the EFDA-JET Workprogramme) 2002 *Plasma Phys. Control. Fusion* **44** 1999
[22] Vincenzi P. *et al* 2023 *Fusion Eng. Des.* **189** 113436
[23] Baiocchi B., Aucone L., Casiraghi I., Figini L., Koechl F. and Mantica P. 2023 *Nucl. Fusion* **63** 106009
[24] Fanale F. *et al* 2024 Status of DTT ECH transmission lines and antennae *IEEE Trans. Plasma Sci.* 1–7
[25] Baiocchi B. *et al* *EC21 Conf.* (*Cadarache, FR, 20–25 June 2022*) p P2.114
[26] Pegourie B., Waller V., Nehme H., Garzotti L. and Géraud A. 2007 *Nucl. Fusion* **47** 44–56
[27] Bourdelle C., Citrin J., Baiocchi B., Casati A., Cottier P., Garbet X. and Imbeaux F. 2016 *Plasma Phys. Control. Fusion* **58** 014036
[28] Artaud J.F. *et al* 2018 *Nucl. Fusion* **58** 105001
[29] Brookman M.W. *et al* 2023 *Nucl. Fusion* **63** 044001
[30] Sysoeva E.V., da Silva F., Gusakov E.Z., Heuraux S. and Popov A.Y. 2015 *Nucl. Fusion* **55** 033016
[31] Snicker A., Poli E., Maj O., Guidi L., Köhn A., Weber H., Conway G., Henderson M. and Saibene G. 2018 *Nucl. Fusion* **58** 016002
[32] Cazabonne J., Coda S., Decker J., Krutkin O., Kumar U. and Peysson Y. (TCV Team) 2024 *Nucl. Fusion* **64** 026019
[33] Casiraghi I. *et al* 2023 *Plasma Phys. Control. Fusion* **65** 035017
[34] Bonanomi N. *et al* *Nucl. Fusion* submitted
[35] Balbinot L., Rubino G. and Innocente P. 2021 *Nucl. Mater. Energy* **27** 100952
[36] Innocente P., Ambrosino R., Brezinsek S., Calabrò G., Castaldo A., Crisanti F., Dose G., Neu R. and Roccella S. 2022 *Nucl. Mater. Energy* **33** 101276
[37] Martin Y.R. *et al* 2008 *J. Phys.: Conf. Ser.* **123** 012033
[38] Vincenzi P. *47th EPS 2021* (*Virtual Conference Stiges (Spain), 21–25 June 2021*) pp 677–80 (available at: https://info.fusion.ciemat.es/OCS/EPS2021PAP/pdf/P3.1057.pdf)
[39] Sertoli M., Angioni C. and Odstrcil T. 2017 *Phys. Plasmas* **24** 112503